Ensemble Riemannian Data Assimilation for High-dimensional Nonlinear Dynamics

Sagar K. Tamang[1,2], Ardeshir Ebtehaj[1,2], Peter J. van Leeuwen[3], Gilad Lerman[4], Efi Foufoula-Georgiou[5,6]

[1]St. Anthony Falls Laboratory, University of Minnesota-Twin Cities, Minnesota, USA
[2]Department of Civil, Environmental and Geo- Engineering, University of Minnesota-Twin Cities, Minnesota, USA
[3]Department of Atmospheric Science, Colorado State University, Fort Collins, Colorado, USA
[4]School of Mathematics, University of Minnesota-Twin Cities, Minnesota, USA
[5]Department of Civil and Environmental Engineering, University of California Irvine, Irvine, California, USA
[6]Department of Earth System Science, University of California Irvine, Irvine, California, USA

Key Points:

- An ensemble data assimilation methodology based on the Wasserstein distance is presented for treating systematic errors in high-dimensional systems.
- The proposed methodology does not require any *a priori* assumption about the shape of the probability distributions.
- To reduce the computational cost, the methodology relies on entropic regularization.

Abstract

This paper presents the results of an ensemble data assimilation methodology over the Wasserstein space for high-dimensional nonlinear dynamical systems, focusing on the chaotic Lorenz-96 model and a two-layer quasi-geostrophic model of atmospheric circulation. Unlike Euclidean data assimilation, this approach is equipped with a Riemannian geometry and formulates data assimilation as a Wasserstein barycenter between the forecast probability distribution and the normalized likelihood function. The methodology does not rely on any Gaussian assumptions and can intrinsically treat systematic model and observation errors. To cope with the computational cost of the Wasserstein distance, the paper examines the efficiency of the entropic regularization. Comparisons with the standard particle and stochastic ensemble Kalman filters demonstrate that under systematic errors the presented methodology could extend the forecast skills of nonlinear dynamical systems.

1 Introduction

The science of data assimilation (DA) aims to optimally combine the information content of observations with forecasts of Earth system models (ESM) to improve the estimation of their initial conditions and thus their predictive capabilities (Kalnay, 2003). Current DA methodologies, either variational (Courtier et al., 1994; A. C. Lorenc, 1986; Poterjoy & Zhang, 2014; Rabier et al., 2000; Zupanski, 1993) or filtering (J. Anderson & Lei, 2013; J. L. Anderson, 2001; Bishop et al., 2001; Janjić et al., 2011; Kalman, 1960; Lei et al., 2018; Tippett et al., 2003), largely rely on penalization of second-order statistics of the unbiased model and observation errors over the Euclidean space. For example, in the three-dimensional variational (3D-Var) DA (Courtier et al., 1998; Z. Li et al., 2013; A. Lorenc et al., 2000; A. C. Lorenc, 1986), a least-squares cost function comprising of weighted Euclidean distances of the state from the previous model forecasts (background state) and the observations is formulated. Solution of this cost function leads to an analysis state, which is a weighted average of the forecasts and observations across multiple dimensions of the problem with the weights dictated by prescribed background and observation error covariance matrices. The variants of the Kalman filtering DA methods (Evensen, 1994a, 2003; Houtekamer & Zhang, 2016; Nerger et al., 2012b; Reichle et al., 2002) also follow the same principle but in these methods, the background covariance contains information from past observations and model evolution.

Apart from the Euclidean distance, other measures and distance metrics including the quadratic mutual information (Kapur, 1994), Kullback-Leibler (KL) divergence (Kullback & Leibler, 1951), Hellinger distance (Hellinger, 1909), and Wasserstein distance (Villani, 2003) have been also utilized in DA frameworks. Among others, Tagade & Ravela (2014) introduced a nonlinear filter, where the analysis is obtained through maximization of the quadratic mutual information. Maclean et al. (2017) utilized the Hellinger distance to measure the difference between the predicted and observed spatial patterns in oceanic flows. Chianese et al. (2018) introduced a variational DA method in which minimization of the KL divergence led to an approximation of the bias terms and model parameters. Similarly, R. Li et al. (2019) employed the KL divergence in an optimization framework to incorporate inequality constraints in the Ensemble Kalman Filter (EnKF, Evensen, 1994b). Recently, Pulido & van

Leeuwen (2019) developed a mapping particle filter in which particles are pushed towards the posterior density by minimizing the KL divergence between the posterior and a series of intermediate probability densities.

In recent years, the Wasserstein or the Earth mover's distance, originating from the theory of optimal mass transport (OMT, B. Chen et al., 2019; Y. Chen et al., 2017, 2018a,b; Kantorovich, 1942; Kolouri et al., 2017; Monge, 1781; Villani, 2003), has been gaining attention in the DA community. Reich (2013) first introduced a new resampling approach in particle filters using the OMT, to maximize the correlation between prior and posterior ensemble members. Ning et al. (2014) further utilized the Wasserstein distance to treat position errors arising from uncertain model parameters. Following on this work, Feyeux et al. (2018) proposed to replace the weighted Euclidean distance with the Wasserstein distance in variational DA frameworks to treat position error. Tamang et al. (2020) proposed to use the Wasserstein distance to regularize a variational DA framework for treating systematic errors arising from the model forecast in chaotic systems. However, DA frameworks utilizing the Wasserstein distance are computationally expensive as they require obtaining a joint distribution that couples two marginal distributions. Finding this joint distribution often relies on interior-point methods (Altman & Gondzio, 1999) or the Orlin's algorithm (Orlin, 1993) that have super-cubic run time – making the Wasserstein DA computationally challenging for high-dimensional geophysical problems. More recently, to reduce the computational cost, Tamang et al. (2021) used entropic regularization of the OMT formulation (Cuturi, 2013) through a new framework, called Ensemble Riemannian Data Assimilation (EnRDA) to cope with systematic biases.

In this paper, we expand EnRDA by testing and documenting its performance over "high-dimensional" nonlinear dynamical systems under systematic errors. Unlike Euclidean DA with a known connection with the family of Gaussian distributions through Bayes' theorem, the EnRDA does not rely on any parametric assumptions about the input probability distributions. Therefore, it does not guarantee an analysis state with a minimum mean squared error. However, as it will be clear later on, it enables to optimally (i) interpolate between the forecast distribution and the normalized likelihood function without any parametric assumptions about their shapes and (ii) formally penalize systematic translations between them arising due to geophysical biases.

The paper poses the hypothesis that under geophysical biases and high-dimensional nonlinear dynamical systems, EnRDA can lead to an analysis state with reduced uncertainty – compared to classic "unbiased" minimum mean-squared error Euclidean DA techniques. To test this hypothesis, we implement EnRDA on the chaotic Lorenz-96 system (Lorenz, 1995) and a two-layer quasi-geostrophic (QG) model (Pedlosky et al., 1987). The results demonstrate that DA over the Wasserstein space provides an alternative approach that may enhance high-dimensional geophysical forecast skills when the distributions of the state variables are not necessarily Gaussian and are corrupted with systematic errors.

The outline of the paper is as follows. Section 2 provides a brief background on optimal mass transport and Wasserstein distance. The EnRDA methodology is presented in Section 3. Section 4 presents different test cases of implementation on the Lorenz-96 and the QG model and documents the performance of the presented approach in comparison with the classic implementation of the standard particle filter with resampling and the Stochastic Ensemble Kalman Filter (SEnKF). A summary and concluding remarks are presented in

Section 5. The details of the entropic regularization for the EnRDA, and covariance inflation and localization procedures for the SEnKF are provided in Appendix A.

2 Background on OMT and the Wasserstein Barycenters

We provide a brief background on the theory of optimal mass transport (OMT) and Wasserstein barycenters. The OMT theory, first put forward by Monge (1781), aims to find the minimum cost of transporting distributed masses of materials from known source points to target points. The theory was later expanded as a new tool to compare probability distributions (Brenier, 1987; Villani, 2003) and since then has found its applications in the field of data assimilation (Feyeux et al., 2018; L. Li et al., 2018; Ning et al., 2014; Tamang et al., 2020), subsurface geophysical inverse problems (J. Chen et al., 2018; Yang & Engquist, 2018; Yang et al., 2018; Yong et al., 2019) and comparisons of climate model simulations (Vissio et al., 2020).

Let us consider a discrete source probability distribution $p(\mathbf{x}) = \sum_{i=1}^{M} p_{\mathbf{x}_i} \delta_{\mathbf{x}_i}$ and a target distribution $p(\mathbf{y}) = \sum_{j=1}^{N} p_{\mathbf{y}_j} \delta_{\mathbf{y}_j}$ with their respective probability masses $\{\mathbf{p}_x \in \mathbb{R}_+^M : \sum_i p_{\mathbf{x}_i} = 1\}$ and $\{\mathbf{p}_y \in \mathbb{R}_+^N : \sum_j p_{\mathbf{y}_j} = 1\}$ supported on m- and n-element column vectors $\mathbf{x}_i \in \mathbb{R}^m$ and $\mathbf{y}_j \in \mathbb{R}^n$, respectively. The notation $\mathbf{p}_x \in \mathbb{R}_+^M$ represents probability masses $\mathbf{p}_x$ containing non-negative real numbers supported on M points, whereas $\delta_{\mathbf{x}}$ is the Dirac function at $\mathbf{x}$. In the Monge formulation, the goal is to seek an optimal surjective transportation map $T^a_{\#}p(\mathbf{x}) = p(\mathbf{y})$ that "pushes forward" the source distribution $p(\mathbf{x})$ towards the target distribution $p(\mathbf{y})$, with a minimum transportation cost as follows:

$$T^a = \underset{T}{\operatorname{argmin}} \sum_{i=1}^{M} c(\mathbf{x}_i, T(\mathbf{x}_i)) \quad \text{s.t. } T^a_{\#}p(\mathbf{x}) = p(\mathbf{y})\,, \tag{1}$$

where $c(\cdot,\cdot) \in \mathbb{R}_+$ represents the cost of transporting a unit mass from one support point in $\mathbf{x}$ to another one in $\mathbf{y}$.

The problem formulation by Monge as expressed in Equation 1, however, is non-convex and the existence of an optimal transportation map is not guaranteed (Y. Chen et al., 2019) – especially, when the number of support points for the target distribution exceeds that of the source distribution ($N > M$) (Peyré et al., 2019). This limitation was overcome by Kantorovich (1942) who introduced a probabilistic formulation of OMT – allowing splitting of probability mass from a single source point to multiple target points. The Kantorovich formalism recasts the OMT problem in a linear programming framework that finds an optimal joint distribution or coupling $\mathbf{U}^a \in \mathbb{R}_+^{M\times N}$ that couples the marginal source and target distributions with the following optimality criterion:

$$\mathbf{U}^a = \underset{\mathbf{U}}{\operatorname{argmin}}\ \operatorname{tr}(\mathbf{C}^{\mathrm{T}}\mathbf{U}) \quad \text{s.t.} \quad \begin{cases} \mathbf{U} \in \mathbb{R}_+^{M\times N} \\ \mathbf{U}\mathbb{1}_N = \mathbf{p}_x \\ \mathbf{U}^{\mathrm{T}}\mathbb{1}_M = \mathbf{p}_y \end{cases}, \tag{2}$$

where $\mathrm{tr}(\cdot)$ is the trace of a matrix, $(\cdot)^{\mathrm{T}}$ is the transposition operator and $\mathbb{1}_M$ represents an M-element column vector of ones. In the above formulation, the known $\{\mathbf{C} \in \mathbb{R}_+^{M\times N} : c_{ij} = \|\mathbf{x}_i - \mathbf{y}_j\|_2^2\}$ denotes the so-called transportation cost matrix which is defined based on the ℓ_2-norm $\|\cdot\|_2$ or the Euclidean distance between the support points of the source and target distributions. Here, the $(i,j)^{\text{th}}$ element u_{ij}^a of optimal joint distribution $\mathbf{U}^a$ represents the respective amount of mass transported from support point $\mathbf{x}_i$ to $\mathbf{y}_j$. Then, the 2-Wasserstein distance or metric between the marginal probability distributions is defined as the square root of the optimal transportation cost $d_{\mathcal{W}}(\mathbf{p}_x, \mathbf{p}_y) = \big(\mathrm{tr}(\mathbf{C}^{\mathrm{T}}\mathbf{U}^a)\big)^{\frac{1}{2}}$ (Dobrushin, 1970; Villani, 2008). It should be noted that due to the linear equality and non-negativity constraints in Equation 2, the family of joint distributions that satisfy these constraints forms a bounded convex polytope (Cuturi & Peyré, 2018) and consequently, the optimal joint distribution $\mathbf{U}^a$ is located on one of the extreme points of such a polytope (Peyré et al., 2019).

Recalling that over the Euclidean space, the barycenter of a group of points is equivalent to their (weighted) mean value. The Wasserstein metric offers a Riemannian generalization of this problem and allows to define the barycenter of a family of probability distributions (Bigot et al., 2012; Rabin et al., 2011; Srivastava et al., 2018). In particular, for a group of K probability mass functions $\mathbf{p}_1, \ldots, \mathbf{p}_K$, a Wasserstein barycenter $\mathbf{p}_\eta$ is defined as their Fréchet mean (Fréchet, 1948) as follows (Agueh & Carlier, 2011):

$$\mathbf{p}_\eta = \underset{\mathbf{p}}{\operatorname{argmin}} \sum_{k=1}^{K} \eta_k d_{\mathcal{W}}^2(\mathbf{p}, \mathbf{p}_k)\,, \tag{3}$$

where $\{(\eta_1, \ldots, \eta_K)^{\mathrm{T}} \in \mathbb{R}_+^K : \sum_k \eta_k = 1\}$ represent the weights associated with the respective distributions. In special cases where the group of K distributions is Gaussian $\{\mathcal{N}(\boldsymbol{\mu}_1, \boldsymbol{\Sigma}_1), \ldots, \mathcal{N}(\boldsymbol{\mu}_K, \boldsymbol{\Sigma}_K)\}$ with mean $\boldsymbol{\mu}_1, \ldots, \boldsymbol{\mu}_K$ and positive definite covariance $\boldsymbol{\Sigma}_1, \ldots, \boldsymbol{\Sigma}_K$, the Wasserstein barycenter is also a Gaussian density $\mathcal{N}(\boldsymbol{\mu}_\eta, \boldsymbol{\Sigma}_\eta)$ with $\boldsymbol{\mu}_\eta = \sum_k \eta_k \boldsymbol{\mu}_k$ and $\boldsymbol{\Sigma}_\eta$ is the unique positive definite root of the matrix equation $\boldsymbol{\Sigma} = \sum_k \eta_k \big(\boldsymbol{\Sigma}^{\frac{1}{2}} \boldsymbol{\Sigma}_k \boldsymbol{\Sigma}^{\frac{1}{2}}\big)^{\frac{1}{2}}$ (Agueh & Carlier, 2011).

3 Ensemble Riemannian Data Assimilation (EnRDA)

Let us assume that the evolution of the i^{th} ensemble member $\mathbf{x}_i \in \mathbb{R}^m$ of ESM simulations can be presented as the following stochastic dynamical system:

$$\mathbf{x}_i^t = \mathcal{M}(\mathbf{x}_i^{t-1}) + \boldsymbol{\omega}_i^t \qquad i = 1, \ldots, M\,, \tag{4}$$

where $\mathcal{M} : \mathbb{R}^m \to \mathbb{R}^m$ is the deterministic nonlinear model operator, evolving the model state in time with a stochastic error term $\boldsymbol{\omega}_i^t \in \mathbb{R}^m$. This dynamical system is observed at time t through an observation equation $\mathbf{y}^t = \mathcal{H}(\mathbf{x}^t) + \boldsymbol{\upsilon}^t$, where $\mathcal{H} : \mathbb{R}^m \to \mathbb{R}^n$ maps the state to the observation space and $\boldsymbol{\upsilon}^t \in \mathbb{R}^n$ represents an additive observation error. Note that the error terms are not necessarily drawn from Gaussian distributions but need to have finite second-order moments.

Hereafter, we drop the time superscript for brevity and represent the model (or background) probability distribution as $p(\mathbf{x}) = \sum_{i=1}^{M} p_{\mathbf{x}_i}\delta_{\mathbf{x}_i}$ with its probability mass vector $\{\mathbf{p}_x \in \mathbb{R}_+^M : \sum_i p_{\mathbf{x}_i} = 1\}$. Furthermore, the normalized likelihood function is represented as $\widetilde{p}(\mathbf{y}|\mathbf{x})$ centered at the given observation $\mathbf{y}$ with its probability mass vector $\{\widetilde{\mathbf{p}}_{y|x} \in \mathbb{R}_+^N : \sum_j \widetilde{p}_{\mathbf{y}|\mathbf{x}_j} = 1\}$. The probability distribution of the analysis state $p(\mathbf{x}_a)$, is then defined as the Wasserstein barycenter between forecast distribution and the normalized likelihood function:

$$p(\mathbf{x}_a) = \underset{p(\mathbf{z})}{\operatorname{argmin}} \left\{ \eta \, d_{\mathcal{W}}^2[\, p(\mathbf{x}), p(\mathbf{z})] + (1-\eta) \, d_{\mathcal{W}}^2[\widetilde{p}(\mathbf{y}|\mathbf{x}),\, p(\mathbf{z})] \right\} , \tag{5}$$

where $\eta \in [0, 1]$ is a displacement parameter that controls the relative weight of the background and observation. The displacement parameter η is a hyperparameter that captures the relative weights of the histogram of the background state and likelihood function in characterization of the analysis state distribution as a Wasserstein barycenter. The optimal value of η needs to be determined offline, using reference data through cross-validation studies. It is important to note that the above formalism requires all dimensions to be observable and thus those dimensions with no observations cannot be updated, which is a limitation of the current formalism compared to the Euclidean DA. This limitation is further discussed later on in Section 5.

To solve the above DA problem, we need to characterize the background distribution and the normalized likelihood function. Similar to the approach used in particle filter (Gordon et al., 1993; van Leeuwen, 2010), we suggest approximating them through ensemble realizations. For constructing the histogram of the normalized likelihood function, we can draw N samples at each assimilation cycle by perturbing the available observation $\mathbf{y}$ with the observation error $\mathcal{N}(0, \mathbf{R})$.

To obtain the Wasserstein barycenter $p(\mathbf{x}_a)$ in Equation 5, we use the McCann's formalism (McCann, 1997; Peyré et al., 2019):

$$p(\mathbf{x}_a) = \sum_{i=1}^{M} \sum_{j=1}^{N} u_{ij}^a \, \delta_{\mathbf{z}_{ij}}, \tag{6}$$

where $\mathbf{z}_{ij} = \eta \, \mathbf{x}_i + (1-\eta) \, \mathbf{y}_j$ represents the support points of the analysis distribution and u_{ij}^a are the elements of the joint distribution $\{\mathbf{U}^a \in \mathbb{R}_+^{M\times N} : \sum_i \sum_j u_{ij} = 1\}$. It is important to note that the analysis state histogram, at each assimilation cycle, is supported on at most $M + N - 1$ points, which is the maximum number of non-zero entries in the optimal joint coupling (Peyré et al., 2019). To keep the number of ensemble members constant throughout, M ensemble members are resampled from $p(\mathbf{x}_a)$ using the multinomial resampling scheme (T. Li et al., 2015).

Computation of the joint distribution in Equation 2 is computationally expensive as explained previously and can be prohibitive for high-dimensional geophysical problems. As suggested by Cuturi (2013), to reduce the computational cost, we regularize the cost function in the optimal transportation plan formulation of EnRDA by a Gibbs-Boltzmann entropy

function:

$$\mathbf{U}^a = \underset{\mathbf{U}}{\operatorname{argmin}}\ \operatorname{tr}(\mathbf{C}^{\mathrm{T}}\mathbf{U}) - \gamma\,\operatorname{tr}\big(\mathbf{U}^{\mathrm{T}}[\log(\mathbf{U} - \mathbb{1}_M\mathbb{1}_N^{\mathrm{T}})]\big) \quad \text{s.t.} \quad \begin{cases} \mathbf{U} \in \mathbb{R}_+^{M\times N} \\ \mathbf{U}\mathbb{1}_N = \mathbf{p}_x \\ \mathbf{U}^{\mathrm{T}}\mathbb{1}_M = \widetilde{\mathbf{p}}_{y|x} \end{cases}, \tag{7}$$

where $\gamma \in \mathbb{R}_+$ is a regularization parameter. The entropic regularization transforms the original OMT formulation to a strictly convex problem, which can then be efficiently solved using Sinkhorn's algorithm (Sinkhorn, 1967). The details of Sinkhorn's algorithm for solving regularized optimal transportation problems are presented in Appendix A.1. The regularization parameter γ balances the solution between the optimal joint distribution and the one that maximizes the relative entropy. It is evident from Equation 7 that at the limit $\gamma \to 0$, the solution of Equation 7 converges to the analysis joint distribution with a minimum morphing cost. However, as the value of γ increases, the convexity of the problem also increases, enabling the deployment of more efficient optimization algorithms than classic solvers of linear programming problems (Dantzig et al., 1955; Orlin, 1993). At the same time, the number of non-zero entries of the joint coupling increases from $M + N - 1$ to MN points as $\gamma \to \infty$, which results in a maximum entropy solution that converges to $\mathbf{U}^a \to \mathbf{p}_x\widetilde{\mathbf{p}}_{y|x}^{\mathrm{T}}$. For a more comprehensive explanation of EnRDA, one can refer to Tamang et al. (2021).

As an example, we examine here the solution of Equation 5 between a banana-shaped distribution denoted by $\mathcal{F}(\xi_1, \xi_2, \xi_3, b) \propto \exp\big(-\xi_1(4 - b\,x_1 - x_2^2) - \xi_2(x_1^2 - \xi_3 x_2^2)\big)$ and a bivariate Gaussian distribution as a function of the displacement parameter $\eta \in [0, 1]$ – resembling the background distribution $p(\mathbf{x})$ and the normalized likelihood function $\widetilde{p}(\mathbf{y}|\mathbf{x})$, respectively with regularization parameter $\gamma = 1000$. As seen from Figure 1, for lower values of η, the analysis state distribution is closer to the observation and its shape resembles the Gaussian distribution. However, as the value of η increases, the analysis state distribution moves closer to the background distribution and starts morphing into a banana-shaped distribution. Therefore, the analysis state distribution is defined as the one that is sufficiently close to the background distribution and the normalized likelihood function not only based on their shape but also their central location – depending on the displacement parameter. Thus, unlike the Euclidean barycenter, this approach does not guarantee that the mean or mode of the analysis state probability distribution is a minimum mean-squared error estimate of the initial condition. In the next section, we present results from systems of well-known dynamics to test the main hypothesis of the paper, that is, to investigate whether EnRDA can lead to an improved approximation of the analysis state under systematic error in high-dimensional nonlinear dynamics, where the distribution of the background state is not necessarily Gaussian.

4 Numerical Experiments and Results

4.1 Lorenz-96

The Lorenz model (Lorenz-96, Lorenz, 1995), which is widely adopted as a testbed for numerous DA experiments (Lguensat et al., 2017; Shen & Tang, 2015; Tang et al., 2014; Tian et al., 2018; Trevisan & Palatella, 2011), offers a simplified representation of the extra-tropical

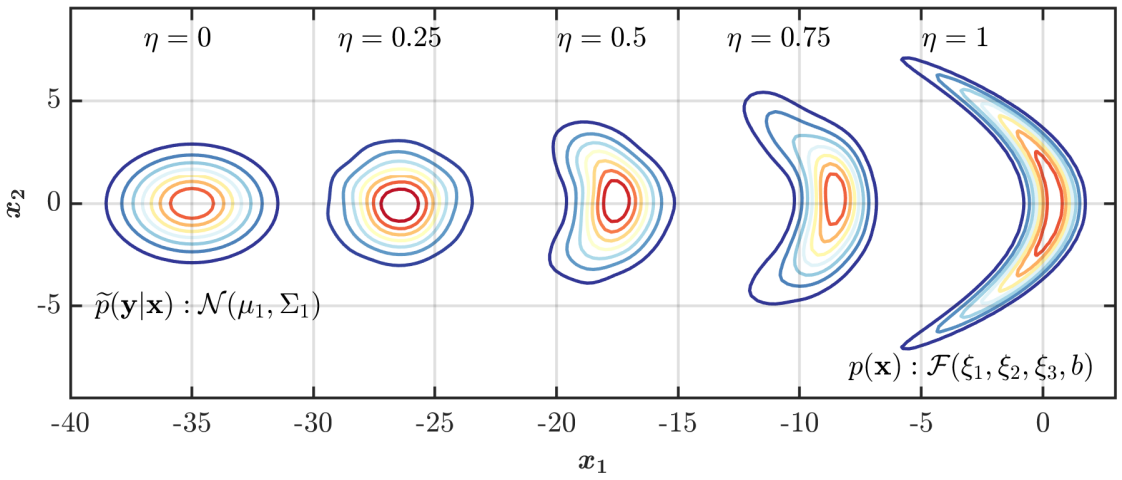

Figure 1: The analysis distribution obtained as a Wasserstein barycenter for different values of the displacement parameter $\eta \in [0, 1]$ between a background distribution represented by a banana-shaped distribution $p(\mathbf{x}) : \mathcal{F}(\xi_1, \xi_2, \xi_3, b)$ with $\xi_1 = 0.02$, $\xi_2 = 0.06$, $\xi_3 = 1.6$, and $b = 8$, and the normalized likelihood function represented by a bivariate Gaussian $\widetilde{p}(\mathbf{y}|\mathbf{x}) : \mathcal{N}(\boldsymbol{\mu}_1, \boldsymbol{\Sigma}_1)$, where $\boldsymbol{\mu}_1 = \begin{bmatrix} -35 \\ 0 \end{bmatrix}$ and $\boldsymbol{\Sigma}_1 = \begin{bmatrix} 3 & 0 \\ 0 & 2 \end{bmatrix}$.

dynamics in the Earth's atmosphere. The model coordinates $\{\mathbf{x} = (x_1, \ldots, x_K)^{\mathrm{T}} \in \mathbb{R}^K\}$ at K dimensions represent the state of an arbitrary atmospheric quantity measured along the Earth's latitudes at K equally spaced longitudinal slices. The model is designed to mimic the continuous-time variation in atmospheric quantities due to interactions between three major components namely advection, internal dissipation, and external forcing. The model dynamics is represented as follows:

$$\frac{dx_k}{dt} = (x_{k+1} - x_{k-2})\, x_{k-1} - x_k + F\,, \qquad k = 1, \ldots, K\,, \tag{8}$$

where $F \in \mathbb{R}_+$ is a constant external forcing independent of the model state. The Lorenz-96 model has cyclic boundaries with $x_{-1} = x_{K-1}$, $x_0 = x_K$, and $x_{K+1} = x_1$. It is known that for small values of $F < 8/9$, the system approaches a steady state condition with each coordinate value converging to the external forcing $x_k \to F$, $\forall k$, whereas for $F > 8/9$, chaos develops (Lorenz & Emanuel, 1998). For standard model setup with $F = 8$, the system is known to exhibit highly chaotic behavior with the largest Lyapunov exponent of 1.67 (Brajard et al., 2020).

4.1.1 Experimental Setup, Results and Discussion

We focus on the 40-dimensional Lorenz-96 system (i.e. $K = 40$) and compare EnRDA results with the classic implementation of the particle filter (PF, Gordon et al., 1993; Poterjoy & Anderson, 2016; Van Leeuwen, 2009; van Leeuwen, 2010) and the Stochastic Ensemble Kalman filter (SEnKF, J. L. Anderson, 2016; Burgers et al., 1998; Evensen, 1994b; Houtekamer & Mitchell, 1998; Janjić et al., 2011; Van Leeuwen, 2020). Similar to the experimental setting suggested in (Lorenz & Emanuel, 1998; Nerger et al., 2012a), we initialize the model by

choosing $x_{20} = 8.008$ and $x_k = 8$ for all other model coordinates. In order to avoid any initial transient effect, the model in Equation 8 is integrated for 1000 time steps using the fourth-order Runge-Kutta approximation (Kutta, 1901; Runge, 1895) with a non-dimensional time step of $\Delta t = 0.01$ and the endpoint of the run is utilized as the initial condition for DA experimentation.

Similar to the suggested experimental setting in (van Leeuwen, 2010), we obtain the ground truth by integrating Equation 8 with a time step of Δt over a time period of $T =$ 0–20 in the absence of any model error. The observations are assumed to be available at each assimilation time interval of $10\Delta t$ and deviated from the ground truth by a Gaussian error $\boldsymbol{\upsilon}_t \sim \mathcal{N}(0, \sigma^2_{\text{obs}}\, \boldsymbol{\Sigma}_\rho)$, with $\sigma^2_{\text{obs}} = 1$ and the correlation matrix $\boldsymbol{\Sigma}_\rho \in \mathbb{R}_+^{40\times 40}$ with 1 on the diagonals, 0.5 on the first sub- and super-diagonals, and 0 everywhere else. The observation time step of $10\Delta t$ is equivalent to 12 hours in global ESMs (Lorenz, 1995).

To characterize the distribution of the background state for each DA methodology, 50 (5000) ensemble members (particles) for the SEnKF and EnRDA (PF) are generated using model errors $\boldsymbol{\omega}_t \sim \mathcal{N}(0, \sigma_t^2\, \mathbf{I}_{40})$ with $\sigma_t^2 = 0.25$ for $t > 0$ and $\sigma_0^2 = 4$, where throughout $\mathbf{I}_m$ represents an $m \times m$ identity matrix. To alleviate the known degeneracy problem in the PF, a higher number of particles was used. Furthermore, to introduce additional systematic background error, we utilize an erroneous external forcing of $F_m = 6$ instead of the "true" forcing value $F = 8$. To have a robust inference, the average values of the error metrics are reported for 50 experiments using different random realizations. As will be elaborated later on, we set the EnRDA displacement parameter $\eta = 0.44$, determined through a cross-validation study based on a minimum mean-squared error criterion. This tuning is similar to tuning inflation and localization parameters in a typical EnKF, or tuning length-scales in 3D- or 4D-Var. Note that we already introduced some systematic error because the truth has zero model error, while the prior does have model errors. In a fully unbiased set up the truth and the prior are drawn from the same distribution.

The results of EnRDA are shown in Figure 2. In the left panel, the temporal evolution of the ground truth and EnRDA analysis state is shown over all dimensions of the Lorenz-96, while a snapshot at time 10 [t] is presented in the right panel. The analysis state obtained from EnRDA follows the ground truth reasonably well during all time steps with a root mean-squared error (rmse) of 0.85. The comparison of EnRDA with the classic implementations of the SEnKF and PF are shown in Figure 3 (a–c). It can be seen that the rmse of the PF increases sharply over time, suggesting that the problem of filter degeneracy still exists despite the higher number of particles. This problem is exacerbated due to the presence of bias causing a rapid collapse of the ensemble variance over time as more particles fall outside of the support set of the likelihood function. The root mean-squared error of both the SEnKF and EnRDA is stabilized over time and is smaller by $\sim$20% (80%) in EnRDA compared to the SEnKF (PF). It is important to note that the presence of systematic bias due to erroneous choice of the external forcing inherently favors EnRDA over SEnKF since the latter is a minimum variance unbiased estimator at the limit $M \to \infty$, where M represents the number of ensemble members.

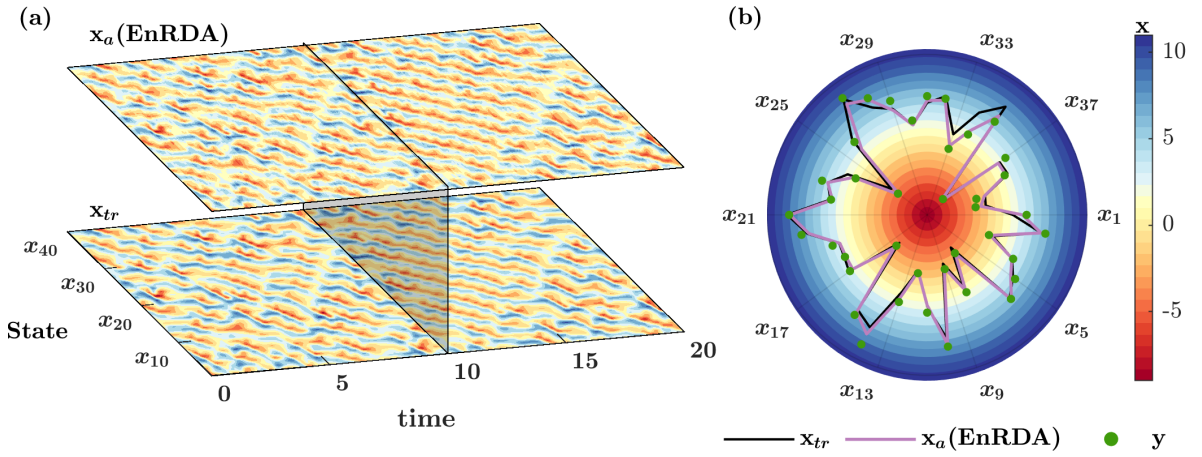

Figure 2: (a) Temporal evolution of the ground truth $\mathbf{x_{tr}}$ and analysis state $\mathbf{x}_a$ by ensemble Riemannian data assimilation (EnRDA) for $K = 40$ dimensions of the Lorenz-96 over $T = 0$–20 [t] and (b) their snapshots at $T = 10$ [t] together with the available observations $\mathbf{y}$.

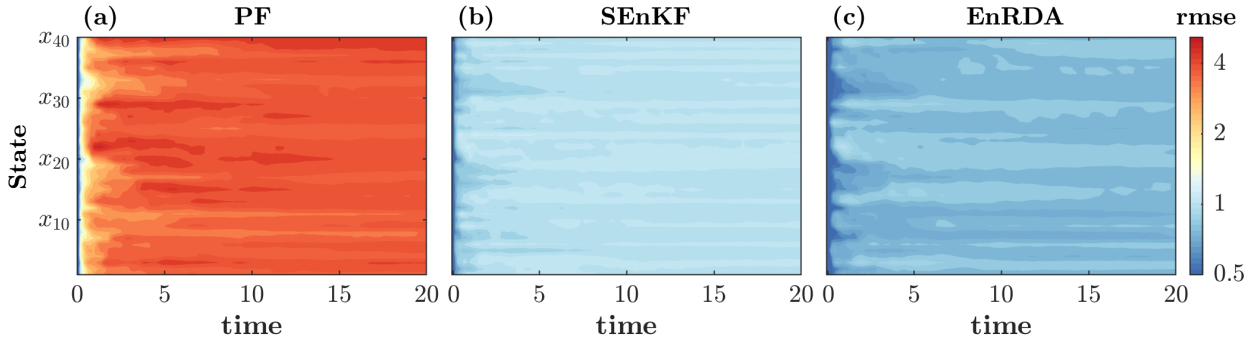

Figure 3: Temporal evolution of the root mean-squared error (rmse) for the (a) Particle Filter (PF) with 5000 particles, (b) Stochastic Ensemble Kalman Filter (SEnKF), and (c) Ensemble Riemannian Data Assimilation (EnRDA) each with 50 ensemble members in 40-dimensional Lorenz-96 system. The results report the mean values of 50 independent simulations.

As previously noted, the displacement parameter η plays an important role in EnRDA as it controls the shape and position of the analysis state distribution relative to the background distribution and the normalized likelihood function. Currently, there exists no known closed-form solution for optimal approximation of this parameter. Therefore, in this paper, we focus on determining its optimal value through heuristic cross-validation by an offline bias-variance trade-off analysis. Specifically, we quantify the rmse of the EnRDA analysis state for different values of η for 50 independent simulations.

The bias and rmse, together with their respective 5^{th}–95^{th} percentile bounds, as functions of the displacement parameter η are shown in Figure 4a. As explained earlier, when η increases, the analysis distribution moves towards the background distribution. Since the background state is systematically biased due to the erroneous external forcing, the analysis bias increases monotonically with η; while the rmse shows a minimum point. Therefore, there exists a form of bias-variance trade-off in the analysis error, which leads to an approximation

of an optimal value of η based on a minimum rmse criterion. It is important to note that the background uncertainty and thus the optimal value of η varies in response to the ensemble size as shown in Figure 4b. The reason is that a larger number of ensemble members reduces the uncertainty in the characterization of the background, but the bias is not affected. To compensate, a larger optimal value for η is needed. This optimal value approaches an asymptotic value as the ensemble sample size increases and will achieve the highest value at the limit $M \to \infty$, when the sample moments converge to the biased forecast moments.

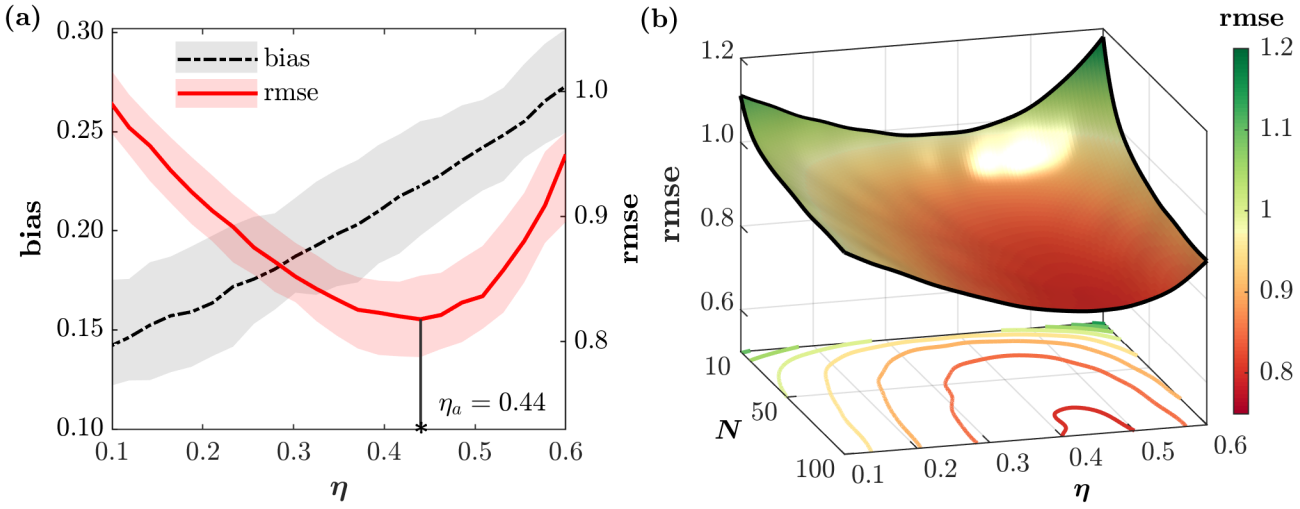

Figure 4: (a) Bias and root mean-squared error (rmse) for a range of displacement parameter $\eta \in [0.1, 0.6]$ in Ensemble Riemannian Data Assimilation (EnRDA) with 50 ensemble members, obtained across 40-dimensions of the Lorenz-96 system. The shaded regions indicate the 5^{th}–95^{th} percentile bound for the respective error metrics obtained from 50 independent simulations. (b) Variation of rmse as a function of the number of ensemble members and η.

One may argue that such a tuning favors EnRDA since it explicitly accounts for the effects of bias, either in background or observations, while there is no bias correction mechanism in the implementation of the SEnKF and the PF. To make a fairer comparison, we investigate an alternative approach to approximate the displacement parameter solely based on the known error covariance matrices at each assimilation cycle. Recalling that in classic DA, the analysis state is essentially the Euclidean barycenter, where the relative weights of the background state and observations are optimally characterized based on the error covariances under zero bias assumptions. However, over the Wasserstein space, the displacement parameter determines the weight between the entire distribution of the background and the normalized likelihood function. Theoretically, knowing the Wasserstein distances from ground truth to both likelihood function and forecast distribution enables to obtain an optimal value for η. Even though such distances are not known in reality, the total Wasserstein distance between the normalized likelihood function and the forecast distribution is known at each assimilation cycle. Therefore, given an estimate of the distance between the ground truth and the normalized likelihood function or the forecast distribution, leads to an approximation of η.

It is known that the square of the Wasserstein distance between two equal-mean Gaus-

sian distributions $\mathcal{N}(\boldsymbol{\mu}, \boldsymbol{\Sigma}_1)$ and $\mathcal{N}(\boldsymbol{\mu}, \boldsymbol{\Sigma}_2)$ is $d^2_{\mathcal{W}} = \mathrm{tr}(\boldsymbol{\Sigma}_1 + \boldsymbol{\Sigma}_2 - 2(\boldsymbol{\Sigma}_1^{\frac{1}{2}}\boldsymbol{\Sigma}_2\boldsymbol{\Sigma}_1^{\frac{1}{2}})^{\frac{1}{2}})$ (Y. Chen et al., 2019). Therefore, under the assumption that only the background state is biased, the square of the Wasserstein distance between the true state $\mathbf{x}_{tr}$, as a Dirac delta function, and the normalized likelihood function reduces to $\mathrm{tr}(\mathbf{R})$. At the same time, the square of the Wasserstein distance between the normalized likelihood function and forecast distribution is $\mathrm{tr}(\mathbf{C}^{\mathrm{T}}\mathbf{U}^a)$. Therefore, we can approximate the interpolation parameter as $\overline{\eta_a} = \mathrm{tr}(\mathbf{R})\left(\mathrm{tr}(\mathbf{C}^{\mathrm{T}}\mathbf{U}^a) + \mathrm{tr}(\mathbf{R})\right)^{-1}$ without any explicit *a priori* knowledge of bias.

Comparisons of the rmse values for the studied DA methodologies as a function of ensemble size are shown in Figure 5. For EnRDA, the displacement parameter is obtained from the bias-aware cross-validation ($\eta = 0.44$, EnRDA-I) and from the known error covariances as explained above (EnRDA-II). The SEnKF and EnRDA result in smaller error metrics with a much smaller ensemble size than PF. As seen, EnRDA can perform well even for smaller ensemble sizes as low as 20. Its results quickly stabilize with more than 40 ensemble members and exhibit a marginal improvement over the SEnKF (12–24%) in the presence of bias. The rmse of the SEnKF also stabilizes quickly but remains above the standard deviation of the observation error indicating that in the presence of bias, the lowest possible variance, known as the Cramer-Rao Lower Bound (Cramér, 1999; Rao et al., 1973) cannot be met.

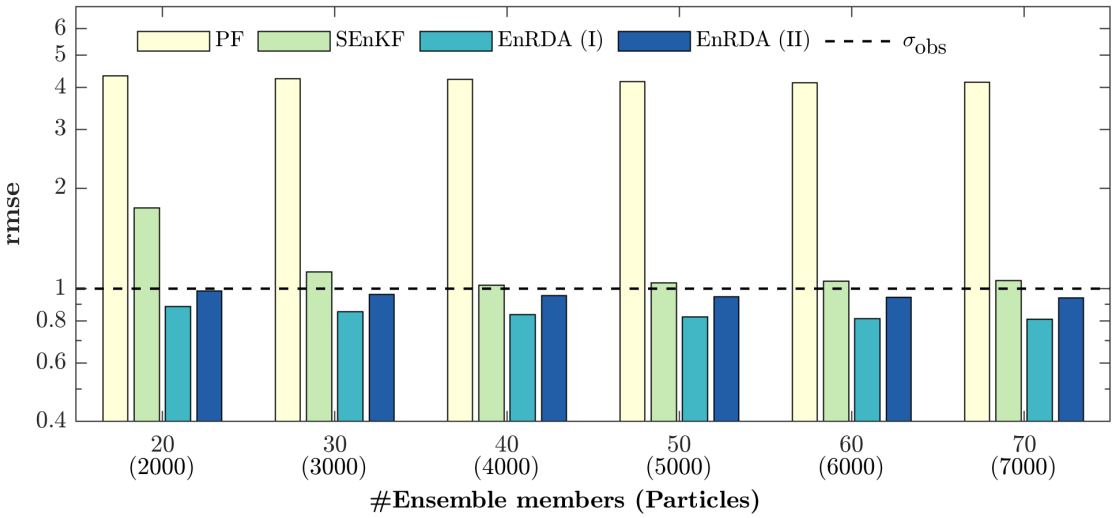

Figure 5: The root mean-squared error (rmse) for the different number of ensemble members/particles in the Particle Filter (PF), Stochastic Ensemble Kalman Filter (SEnKF), and Ensemble Riemannian Data Assimilation (EnRDA) when the displacement parameter is obtained from bias-aware cross-validation (ENRDA-I) and a dynamic approach without *a priori* knowledge of bias (EnRDA-II) for Lorenz-96 system. The dashed line is the standard deviation of the observation error.

It is also important to note that the higher rmse of the PF compared to the SEnKF and EnRDA is due to the problem of filter degeneracy which is further exacerbated by the presence of systematic errors in model forecasts (Poterjoy & Anderson, 2016). To alleviate this problem, one may investigate the use of methodologies suggested in recent years including the auxiliary particle filter where the weights of the particles at each assimilation cycle are

defined based on the likelihood function from the next cycle using a pre-model run (Pitt & Shephard, 1999), the backtracking particle filter in which the analysis state is backtracked to identify the time step when the filter became degenerate (Spiller et al., 2008) as well as sampling from a transition density to pull back particles towards observations (van Leeuwen, 2010).

4.2 Quasi-Geostrophic Model

The multilayered quasi-geostrophic (QG, Pedlosky et al., 1987) model is known as one of the simplest circulation models capable of providing a reasonable representation of the mesoscale variability in geophysical flows. In its simplified form, the QG model describes the conservation of potential vorticity $\{\zeta_k\}_{k=1}^{K}$ in K vertically-mixed vertical layers:

$$\left(\frac{\partial}{\partial t} + u_k\frac{\partial}{\partial \lambda} + v_k\frac{\partial}{\partial \phi}\right)\zeta_k = 0\,, \qquad k = 1, \ldots, K\,, \tag{9}$$

where $u_k = -\dfrac{\partial \Psi_k}{\partial \phi}$ and $v_k = \dfrac{\partial \Psi_k}{\partial \lambda}$ represent the zonal and meridional components of the velocity field, obtained from the geostrophic approximation; $\{\Psi_k\}_{k=1}^{K}$ is the streamfunction in K layers; and λ and ϕ are the zonal and meridional coordinates, respectively.

For a two-layer QG model ($K = 2$), the potential vorticity at any time step is the sum of the relative vorticity, the planetary vorticity and the stretching term, given by:

$$\zeta_k = \nabla^2\Psi_k + f + (1 - 2\delta_{2k})\frac{f_0^2}{g'h_k}(\Psi_2 - \Psi_1) \qquad k = 1, \ldots, 2\,, \tag{10}$$

where $\nabla^2(\cdot) = \dfrac{\partial^2(\cdot)}{\partial \lambda^2} + \dfrac{\partial^2(\cdot)}{\partial \phi^2}$ is the Laplace operator, $f = f_0 + \beta(\phi - \phi_0)$ is the Coriolis parameter linearly varying with the meridional coordinate ϕ (β-plane approximation), f_0 is the Coriolis parameter at mid-basin where $\phi = \phi_0$, $g' = \dfrac{g(\rho_2 - \rho_1)}{\rho_2}$ is the reduced value of the gravitational acceleration g, ρ_k and h_k are the density and thickness of the k^{th} layer, respectively. The QG model has been the subject of numerous experiments to test the performance of DA techniques (Cotter et al., 2020; Evensen, 1994b; Evensen & Van Leeuwen, 1996; Fisher & Gürol, 2017; Penny et al., 2019).

4.2.1 Experimental Setup, Results and Discussion

Due to the high-dimensionality of the QG model and the well-known problem of filter degeneracy in the PF, we chose to omit its application on the QG model. Similar to the study conducted in (Evensen, 1992, 1994b), the streamfunction is chosen as the state variable for the DA experiments. The streamfunction field, at each vertical layer, is discretized over a uniform grid of dimension $m_\lambda \times m_\phi$ with spacing of $\Delta\lambda = \Delta\phi = 100$ km, where $m_\lambda = 65$ and $m_\phi = 33$. The model domain is assumed to have periodic boundaries along the zonal direction and free-slip conditions, that is, $v_k = 0, \forall k$, holds on the northern and southern boundaries. The standard model parameter values of $f_0 = 7.28 \times 10^{-5}$ s^{-1}, $\beta = 2 \times 10^{-11}$ m^{-1} s^{-1}, and

$g = 9.81$ m s^{-2} are used. The total depth of the atmospheric column is set to 10 km with depths and densities of top and bottom layer as $h_1 = h_2 = 5$ km, and $\rho_1 = 1$ and $\rho_2 = 1.05$ kg m^{-3}, respectively. We first initialize the streamfunction in the two layers as a function of the zonal and meridional coordinates by setting $\Psi_1(\lambda, \phi) = -12.5 \times 10^6 \tan^{-1}\left(20(\phi/\Delta\phi - m_\phi/2)m_\phi^{-1}\right) - 1.25 \times 10^6 \sin\left(2\pi(\lambda/\Delta\lambda - 1)m_\lambda{}^{-1}\right) \sin^2\left(2\pi(\phi/\Delta\phi - 1)(m_\phi - 1)^{-1}\right)$ m^2 s^{-1} and $\Psi_2(\lambda, \phi) = 0.3\, \Psi_1(\lambda, \phi)$.

From the initial value of the streamfunction field in each layer, potential vorticity is obtained using a nine-point second-order finite difference scheme to compute the Laplacian in Equation 10. The model in Equation 9 is then integrated with a time step of $\Delta t = 0.5$ hr using the fourth-order Runge-Kutta approximation to advect and obtain potential vorticity at internal grid points for the next time step. The streamfunction at the next time step is then calculated from this potential vorticity by solving the set of the Helmholtz equations (Equation 10). To avoid any form of initial transient behavior and to create vortex structures in the streamfunction, the QG model is integrated first for 720 time steps and then the endpoint of the run is used as the initial condition for subsequent DA experimentation.

The ground truth of the streamfunction is obtained by integrating the QG model with a time step of Δt over a time period of $T = 0 - 15$ day in the absence of any model error. Observations are assumed to be available at an assimilation time interval of $24\Delta t$ or 12 hr. To construct observations, representative, random and systematic errors are applied to the ground truth. The representative error is applied by lowering the resolution of the ground truth through box averaging over a window of size $n_\lambda \times n_\phi$, where $n_\lambda = 5$ and $n_\phi = 3$. Then a heteroscedastic biased Gaussian noise with mean (standard deviation) 0.6×10^6 m^2 s^{-1}, equivalent to 33 (10%) of the mean magnitude of the ground truth is applied.

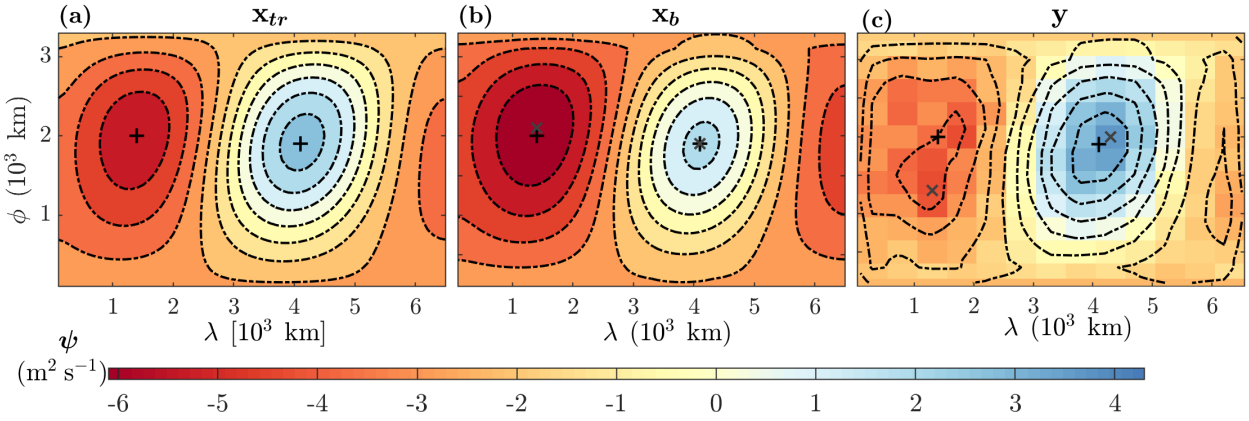

Figure 6: (a) The true state $\mathbf{x}_{tr}$, (b) background state $\mathbf{x}_b$, and (c) observations $\mathbf{y}$ for bottom layer field of streamfunction in the quasi-geostrophic model at first assimilation cycle $T = 12$ hr. The black plus (grey cross) signs show the location of the global extrema for the true state (background and observation).

To characterize the distribution of the background state, 50 ensemble members for both SEnKF and EnRDA are generated using model errors $\boldsymbol{\omega}_t \sim \mathcal{N}(0, \alpha\, \sigma_t^2\, \mathbf{I}_{m_\lambda \times m_\phi})$ for each layer with $\sigma_0^2 = 10^8$ m^4 s^{-2} and $\sigma_t^2 = 5 \times 10^6$ m^4 s^{-2} for $t > 0$, where the factor $\alpha \in [0, 1]$ grows linearly from 0 at the northern and southern boundaries to 1 at mid-basin. To introduce

systematic errors in the forecast, we utilize a multiplicative error of 0.015% in the QG model by multiplying the potential vorticity obtained from Equation 10 at every Δt with a factor of 1.00015. At each assimilation cycle, $N = 500$ samples of the observations are obtained by perturbing the observations with the heteroscedastic Gaussian noise with standard deviation 10% of the mean magnitude of the ground truth.

In the SEnKF, to alleviate the well-known problem of undersampling (J. L. Anderson, 2012) and improve its performance, we utilize covariance inflation (J. L. Anderson & Anderson, 1999) and localization (Hamill, 2001; Houtekamer & Mitchell, 2001) as discussed in Appendix A.2. For EnRDA, similar to the Lorenz-96 setup (Section 4.1.1), the displacement parameter is set to $\eta = 0.4$ through a cross-validation study based on a minimum rmse criterion as shown in Table 1. To increase the robustness of the inference about the results, the quality metrics are averaged using 10 simulations with different random realizations.

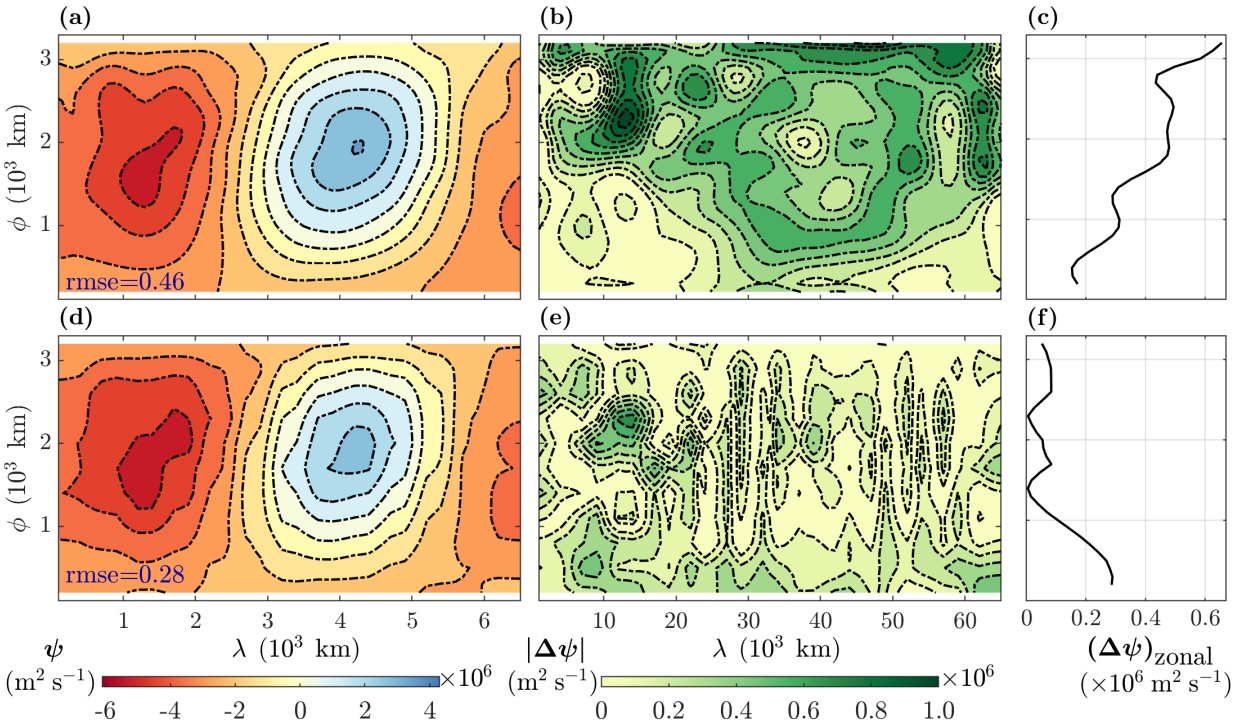

Figure 7: The streamfunction analysis state $\mathbf{x}_a$ by (a) Stochastic Ensemble Kalman Filter (SEnKF), and (d) Ensemble Riemannian Data Assimilation (EnRDA) as well as (b, e) their respective absolute error fields and (c, f) zonal mean of the error for the bottom layer of quasi-geostrophic model, at the first assimilation cycle $T = 12$ hr. The root mean-squared error (rmse) values ($\times 10^6$ m^2 s^{-1}) for the entire fields are also reported in (a) and (d).

The true state, background state, and the observations of the bottom layer streamfunction at the first assimilation cycle $T = 12$ hr are shown in Figure 6. It can be seen that both the background state and the observations show possible systematic biases as the position and the values of their global extrema are significantly different from the ground truth.

The results of the DA experiments using the SEnKF and EnRDA at the first assimilation cycle for the bottom layer are also shown in Figure 7. It can be seen that, in the SEnKF, the streamfunction values are slightly overestimated, signaling the persistence of bias in the

Table 1: Average root mean-squared error (rmse) values as a function of the displacement parameter $\eta \in [0.25, 0.6]$ for Ensemble Riemannian Data Assimilation (EnRDA) from 10 independent simulations of the two-layer quasi-geostrophic model.

rmse ($\times 10^6$ m^2 s^{-1})								
η	0.25	0.30	0.35	0.40	0.45	0.50	0.55	0.60
Top layer	0.283	0.260	0.255	0.242	0.250	0.258	0.309	0.369
Bottom layer	0.211	0.198	0.194	0.189	0.206	0.222	0.294	0.368
Average	0.247	0.229	0.224	0.215	0.228	0.240	0.301	0.369

analysis state (Figure 7a). This is further evident as the analysis error field is coherent and structured (Figure 7b). On the other hand, it appears that EnRDA (Figure 7d) results in a more incoherent error field with a reduced bias (Figure 7e). The rmse for the EnRDA (0.28×10^6 m^2 s^{-1}) is lower than the one by the SEnKF (0.46×10^6 m^2 s^{-1}). However, the difference between the two methods shrinks over $T = 0-15$ days and the mean analysis rmse over both layers by the EnRDA (SEnKF) reaches 0.21×10^6 (0.25×10^6) m^{2}s^{-1}. Furthermore, in the SEnKF, due to the presence of systematic error, the zonal mean of the absolute error is consistently higher than that of the EnRDA, see (Figure 7c and f).

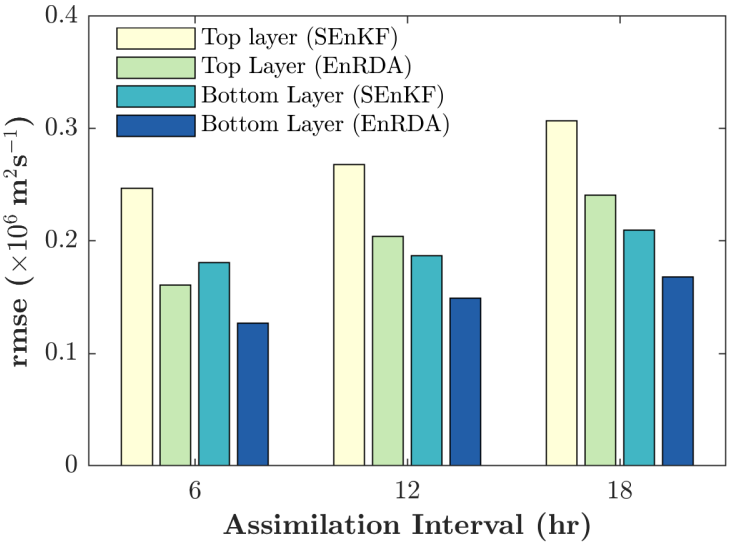

Figure 8: The average root mean-squared error (rmse) values as a function of assimilation intervals 6, 12 and 18 hr in the Stochastic Ensemble Kalman Filter (SEnKF) and Ensemble Riemannian Data Assimilation (EnRDA) for the two-layer quasi-geostrophic model.

We further examined the performance of the EnRDA and the SEnKF on the QG model with a $\pm 50\%$ change in the assimilation interval of 12 hr as shown in Figure. 8. To make the comparison fair between different assimilation intervals which have a different number of assimilation cycles and to eliminate the impact of transient behavior, we only report the statistics for the last 15 assimilation steps. With the increase in assimilation interval, the

systematic error grows in the forecast largely due to the multiplicative error being added to the forecast at every time step. Therefore, as is expected, with the increase in assimilation interval, the rmse grows monotonically and the performance of the DA methodologies degrades. However, the EnRDA demonstrates consistent improvement over a bias-blind implementation of the SEnKF (20–33%) across the range of assimilation intervals.

5 Summary and Concluding Remarks

In this study, we discussed recasting geophysical data assimilation (DA) as a barycenter problem over the Wasserstein space with Riemannian geometry, in an ensemble setting. The DA methodology, called the Ensemble Riemannian Data Assimilation (EnRDA), enables to obtain the analysis state probability distribution through optimal transportation of probability masses between the background distribution and the normalized likelihood function. We demonstrated that this approach does not rely on any parametric assumptions about the distributions. Unlike DA over the Euclidean space, this approach does not guarantee a minimum mean squared approximation of the analysis when the model and observations are unbiased. However, it can formally correct systematic errors by allowing for a smooth transition between the background distribution and the normalized likelihood function over the Wasserstein space. Therefore, we hypothesized that under a biased state space, EnRDA can lead to reduced uncertainty of the analysis state compared to classic DA over the Euclidean space with no ad-hoc bias correction.

We verified the hypothesis by applying the EnRDA to the 40-dimensional chaotic Lorenz-96 system and a two-layer quasi-geostrophic representation of atmospheric circulation. Although initial comparisons of EnRDA with classic DA methodologies, in our case, the Stochastic Ensemble Kalman Filter and the Particle Filter, suggested improved performance, further comprehensive comparisons with bias-aware versions of the Euclidean DA methodologies are required to fully characterize the pros and cons of DA over the Wasserstein space. We need to emphasize that in the absence of systematic errors, Euclidean DA methodologies is likely to achieve improved performance over EnRDA in terms of the mean squared error. However, one of the advantages of the EnRDA is that it is a fully nonlinear DA method, and it does not require any localization procedure.

One of the major weaknesses of the presented methodology in its current form is that all dimensions of the problem are assumed to be observable. This is an important issue when it comes to the assimilation of sparse data. Future research is needed to address partial observability in DA over the Wasserstein space. A possible direction is through multi-marginal optimal mass transport (Pass, 2015), which could enable to couple different dimensions of the problem and propagate the information content of sparse observations to unobserved dimensions. Moreover, currently, the displacement parameter is constant across multiple dimensions of the problem. Future research is needed to understand how the displacement parameter can be estimated differently depending on the error structure across different dimensions of the state space. Another option is to perform the EnRDA only in that part of the state space that is directly observed and use the ensemble covariance to update the unobserved part of state space, similar to a SEnKF. We anticipate that expanding the application of the presented methodology for assimilating satellite data into land-atmosphere

models could be another useful future direction of research given the fact that these models are often markedly biased (Chepurin et al., 2005; Dee & Da Silva, 1998; De Lannoy et al., 2007; Lin et al., 2017).

A Appendix

A.1 Sinkhorn's Algorithm for Optimal Mass Transport

To solve the regularized optimal mass transport problem in Equation 7, we utilize Sinkhorn's algorithm (Sinkhorn, 1967). To that end, first, the Lagrangian form of the Equation 7 using two Lagrange multipliers $\mathbf{a} \in \mathbb{R}^M$ and $\mathbf{b} \in \mathbb{R}^N$ is obtained as follows:

$$\mathcal{L}(\mathbf{U}, \mathbf{a}, \mathbf{b}) = \mathrm{tr}(\mathbf{C}^{\mathrm{T}}\mathbf{U}) - \gamma \mathrm{tr}\big(\mathbf{U}^{\mathrm{T}}[\log(\mathbf{U} - \mathbb{1}_M \mathbb{1}_N^{\mathrm{T}})]\big) - \mathbf{a}^{\mathrm{T}}(\mathbf{U}\mathbb{1}_N - \mathbf{p}_x) - \mathbf{b}^{\mathrm{T}}(\mathbf{U}^{\mathrm{T}}\mathbb{1}_M - \widetilde{\mathbf{p}}_{y|x})\,. \quad (11)$$

Now, we set the first-order derivative of the Lagrangian form in Equation 11, with respect to $(i, j)^{\text{th}}$ element of the joint distribution (u_{ij}) to zero:

$$\frac{\partial \mathcal{L}(\mathbf{U}, \mathbf{a}, \mathbf{b})}{\partial\, u_{ij}} = c_{ij} + \gamma \log(u_{ij}) - a_i - b_j = 0 \qquad \forall i, j\,, \quad (12)$$

which ultimately leads to $u_{ij} = \exp\left(\frac{a_i}{\gamma}\right) \exp\left(-\frac{c_{ij}}{\gamma}\right) \exp\left(\frac{b_j}{\gamma}\right)$. This can be rewritten in a matrix form as $\mathbf{U}^a = \mathrm{diag}(\mathbf{s})\mathbf{V}\,\mathrm{diag}(\mathbf{t})$, where $\left\{\mathbf{V} \in \mathbb{R}_+^{M\times N} : v_{ij} = \exp\left(-\frac{c_{ij}}{\gamma}\right)\right\}$ is the Gibb's kernel of the cost matrix $\mathbf{C}$, and $\mathbf{s} \in \mathbb{R}^M$, $\mathbf{t} \in \mathbb{R}^N$ are the unknown scaling vectors. The notation $\mathrm{diag}(\mathbf{x}) \in \mathbb{R}^{M\times M}$ represents a diagonal matrix with its diagonal entries provided by $\mathbf{x} \in \mathbb{R}^M$.

By setting the derivatives of the Lagrangian with respect to the Lagrange multipliers as zero we recover the two conditions, which we can write as $\mathbf{p}_x = \mathrm{diag}(\mathbf{s})\mathbf{V}\,\mathrm{diag}(\mathbf{t})\mathbb{1}_N$ and $\widetilde{\mathbf{p}}_{y|x} = \mathrm{diag}(\mathbf{t})\mathbf{V}^{\mathrm{T}}\,\mathrm{diag}(\mathbf{s})\mathbb{1}_M$ leading to:

$$\mathbf{s} = \mathbf{p}_x \oslash (\mathbf{V}\,\mathbf{t}) \qquad \text{and} \qquad \mathbf{t} = \widetilde{\mathbf{p}}_{y|x} \oslash (\mathbf{V}^{\mathrm{T}}\,\mathbf{s})\,, \quad (13)$$

where the notation $\mathbf{x} \oslash \mathbf{y}$ represents a Hadamard element-wise division of equal length vectors. The form presented in Equation 13 is known as the matrix scaling problem (Borobia & Cantó, 1998) and can be efficiently solved iteratively:

$$\mathbf{s}^{(i)} = \mathbf{p}_x \oslash (\mathbf{V}\,\mathbf{t}^{(i-1)}) \qquad \text{and} \qquad \mathbf{t}^{(i)} = \widetilde{\mathbf{p}}_{y|x} \oslash (\mathbf{V}^{\mathrm{T}}\,\mathbf{s}^{(i)})\,, \quad (14)$$

where i is the iteration count and the algorithm is initialized with a positive vector $\mathbf{t}^{(0)} = \mathbb{1}_N$. In our implementation, we set the iteration termination criterion as $\frac{\left\|\mathbf{s}^{(i)} - \mathbf{s}^{(i-1)}\right\|_2}{\left\|\mathbf{s}^{(i-1)}\right\|_2} \leq 10^{-4}$ or $i > 300$. After the convergence of the solution for $\mathbf{s}$ and $\mathbf{t}$, the optimal joint distribution can be obtained as $\mathbf{U}^a = \mathrm{diag}(\mathbf{s})\mathbf{V}\,\mathrm{diag}(\mathbf{t})$.

A.2 Covariance Inflation and Localization in Ensemble Kalman Filter

The ensemble size in the Stochastic Ensemble Kalman filter (SEnKF), if much smaller than the state dimension, such as in the presented case of the quasi-geostrophic model, leads to underestimation of the forecast error covariance matrix and subsequently filter divergence problems. To alleviate this problem, a covariance inflation procedure can be implemented by multiplying the forecast error covariance matrix by an inflation factor $\tau > 1$ (J. L. Anderson & Anderson, 1999) where its optimal value depend on the ensemble size (Hamill et al., 2001) and other characteristics of the problem at hand.

The covariance localization procedure in the SEnKF further attempts to improve its performance by ignoring the spurious long-range dependence in the ensemble background covariance by applying a prespecified cutoff threshold on the correlation structure of the field. An SEnKF equipped with a tuned localization procedure can be efficiently used in high-dimensional atmospheric and ocean models even with less than 100 ensemble members (J. L. Anderson, 2012). The covariance localization in an SEnKF is accomplished by modifying the Kalman gain matrix $\mathbf{K} \in \mathbb{R}^{m\times m}$ through implementation of a Hadamard element-wise product of the forecast error covariance matrix $\mathbf{B} \in \mathbb{R}^{m\times m}$ with a distance-based correlation matrix $\boldsymbol{\rho} \in \mathbb{R}^{m\times m}$:

$$\mathbf{K} = (\boldsymbol{\rho} \odot \mathbf{B})\mathbf{H}^{\mathrm{T}}\big(\mathbf{H}(\boldsymbol{\rho} \odot \mathbf{B})\mathbf{H}^{\mathrm{T}} + \mathbf{R}\big)^{-1}, \tag{15}$$

where $\mathbf{X} \odot \mathbf{Y}$ represent the Hadamard element-wise product between equal size matrices $\mathbf{X}$ and $\mathbf{Y}$.

Following the work of Gaspari & Cohn (1999), we utilized the fifth-order piece-wise rational function that depends on a single length scale parameter d and an Euclidean distance matrix $\{\mathbf{L} \in \mathbb{R}^{m\times m} : l_{ij} = \|x_i - x_j\|_2\}$ for obtaining the $(i,j)^{\text{th}}$-element of the localizing correlation matrix $\boldsymbol{\rho}$:

$$\rho_{ij} = \begin{cases} -\frac{1}{4}r^5 + \frac{1}{2}r^4 + \frac{5}{8}r^3 - \frac{5}{3}r^2 + 1, & 0 \le r \le 1\,, \\ \frac{1}{12}r^5 - \frac{1}{2}r^4 + \frac{5}{8}r^3 + \frac{5}{3}r^2 - 5r + 4 - \frac{2}{3}r^{-1}, & 1 < r \le 2\,, \\ 0\,, & r > 2\,, \end{cases} \tag{16}$$

where $r = \dfrac{l_{ij}}{d}$, and d is the length scale.

In our implementation of the SEnKF in the QG model, the inflation factor and length scale were chosen between $\tau = 1.01-1.08$ and $d = 400-1800$ [km] respectively depending on the experimental setup through trial and error analysis to minimize the root mean-squared error.

Acknowledgements

Data archiving is underway at the Data Repository for University of Minnesota (`https://conservancy.umn.edu/handle/11299/166578`). The first and second author acknowledge the grant from the National Aeronautics and Space Administration (NASA) Terrestrial Hydrology Program (THP, 80NSSC18K1528) and the New (Early Career) Investigator Program (NIP, 80NSSC18K0742). The third author acknowledges support from the European Research Council for funding via the Horizon2020 CUNDA project under number 694509. The fourth author also acknowledges support from National Science Foundation (NSF, DMS1830418).

References

Agueh, M., & Carlier, G. (2011). Barycenters in the wasserstein space. *SIAM Journal on Mathematical Analysis*, *43*(2), 904–924.

Altman, A., & Gondzio, J. (1999). Regularized symmetric indefinite systems in interior point methods for linear and quadratic optimization. *Optimization Methods and Software*, *11*(1-4), 275–302.

Anderson, J., & Lei, L. (2013). Empirical localization of observation impact in ensemble kalman filters. *Monthly Weather Review*, *141*(11), 4140–4153.

Anderson, J. L. (2001). An ensemble adjustment kalman filter for data assimilation. *Monthly weather review*, *129*(12), 2884–2903.

Anderson, J. L. (2012). Localization and sampling error correction in ensemble kalman filter data assimilation. *Monthly Weather Review*, *140*(7), 2359–2371.

Anderson, J. L. (2016). Reducing correlation sampling error in ensemble kalman filter data assimilation. *Monthly Weather Review*, *144*(3), 913–925.

Anderson, J. L., & Anderson, S. L. (1999). A monte carlo implementation of the nonlinear filtering problem to produce ensemble assimilations and forecasts. *Monthly Weather Review*, *127*(12), 2741–2758.

Bigot, J., Klein, T., et al. (2012). Consistent estimation of a population barycenter in the wasserstein space. *ArXiv e-prints*, *49*.

Bishop, C. H., Etherton, B. J., & Majumdar, S. J. (2001). Adaptive sampling with the ensemble transform kalman filter. part i: Theoretical aspects. *Monthly weather review*, *129*(3), 420–436.

Borobia, A., & Cantó, R. (1998). Matrix scaling: A geometric proof of sinkhorn's theorem. *Linear algebra and its applications*, *268*, 1–8.

Brajard, J., Carrassi, A., Bocquet, M., & Bertino, L. (2020). Combining data assimilation and machine learning to emulate a dynamical model from sparse and noisy observations: a case study with the lorenz 96 model. *Journal of Computational Science*, *44*, 101171.

Brenier, Y. (1987). Décomposition polaire et réarrangement monotone des champs de vecteurs. *CR Acad. Sci. Paris Sér. I Math.*, *305*, 805–808.

Burgers, G., Jan van Leeuwen, P., & Evensen, G. (1998). Analysis scheme in the ensemble kalman filter. *Monthly weather review*, *126*(6), 1719–1724.

Chen, B., Dang, L., Gu, Y., Zheng, N., & Prıncipe, J. C. (2019). Minimum error entropy kalman filter. *arXiv preprint arXiv:1904.06617*.

Chen, J., Chen, Y., Wu, H., & Yang, D. (2018). The quadratic wasserstein metric for earthquake location. *Journal of Computational Physics*, *373*, 188–209.

Chen, Y., Georgiou, T. T., & Tannenbaum, A. (2017). Matrix optimal mass transport: a quantum mechanical approach. *IEEE Transactions on Automatic Control*, *63*(8), 2612–2619.

Chen, Y., Georgiou, T. T., & Tannenbaum, A. (2018a). Optimal transport for gaussian mixture models. *IEEE Access*, *7*, 6269–6278.

Chen, Y., Georgiou, T. T., & Tannenbaum, A. (2018b). Wasserstein geometry of quantum states and optimal transport of matrix-valued measures. In *Emerging applications of control and systems theory* (pp. 139–150). Springer.

Chen, Y., Georgiou, T. T., & Tannenbaum, A. (2019). Optimal transport for gaussian mixture models. *IEEE Access*, *7*, 6269–6278.

Chepurin, G. A., Carton, J. A., & Dee, D. (2005). Forecast model bias correction in ocean data assimilation. *Monthly weather review*, *133*(5), 1328–1342.

Chianese, E., Galletti, A., Giunta, G., Landi, T., Marcellino, L., Montella, R., & Riccio, A. (2018). Spatiotemporally resolved ambient particulate matter concentration by fusing observational data and ensemble chemical transport model simulations. *Ecological Modelling*, *385*, 173–181.

Cotter, C., Crisan, D., Holm, D., Pan, W., & Shevchenko, I. (2020). Modelling uncertainty using stochastic transport noise in a 2-layer quasi-geostrophic model. *Foundations of Data Science*, *2*(2), 173.

Courtier, P., Andersson, E., Heckley, W., Vasiljevic, D., Hamrud, M., Hollingsworth, A., ... Pailleux, J. (1998). The ecmwf implementation of three-dimensional variational assimilation (3d-var). i: Formulation. *Quarterly Journal of the Royal Meteorological Society*, *124*(550), 1783–1807.

Courtier, P., Thépaut, J.-N., & Hollingsworth, A. (1994). A strategy for operational implementation of 4d-var, using an incremental approach. *Quarterly Journal of the Royal Meteorological Society*, *120*(519), 1367–1387.

Cramér, H. (1999). *Mathematical methods of statistics* (Vol. 9). Princeton university press.

Cuturi, M. (2013). Sinkhorn distances: Lightspeed computation of optimal transport. In *Advances in neural information processing systems* (pp. 2292–2300).

Cuturi, M., & Peyré, G. (2018). Semidual regularized optimal transport. *SIAM Review*, *60*(4), 941–965.

Dantzig, G. B., Orden, A., Wolfe, P., et al. (1955). The generalized simplex method for minimizing a linear form under linear inequality restraints. *Pacific Journal of Mathematics*, *5*(2), 183–195.

Dee, D. P., & Da Silva, A. M. (1998). Data assimilation in the presence of forecast bias. *Quarterly Journal of the Royal Meteorological Society*, *124*(545), 269–295.

De Lannoy, G. J., Reichle, R. H., Houser, P. R., Pauwels, V., & Verhoest, N. E. (2007). Correcting for forecast bias in soil moisture assimilation with the ensemble kalman filter. *Water Resources Research*, *43*(9).

Dobrushin, R. L. (1970). Prescribing a system of random variables by conditional distributions. *Theory of Probability & Its Applications*, *15*(3), 458–486.

Evensen, G. (1992). Using the extended kalman filter with a multilayer quasi-geostrophic ocean model. *Journal of Geophysical Research: Oceans*, *97*(C11), 17905–17924.

Evensen, G. (1994a). Sequential data assimilation with a nonlinear quasi-geostrophic model using Monte Carlo methods to forecast error statistics. *Journal of Geophysical Research*, *99*(C5), 10143. Retrieved from `http://doi.wiley.com/10.1029/94JC00572` doi: 10.1029/94JC00572

Evensen, G. (1994b). Sequential data assimilation with a nonlinear quasi-geostrophic model using monte carlo methods to forecast error statistics. *Journal of Geophysical Research: Oceans*, *99*(C5), 10143–10162.

Evensen, G. (2003). The ensemble kalman filter: Theoretical formulation and practical implementation. *Ocean dynamics*, *53*(4), 343–367.

Evensen, G., & Van Leeuwen, P. J. (1996). Assimilation of geosat altimeter data for the agulhas current using the ensemble kalman filter with a quasigeostrophic model. *Monthly Weather Review*, *124*(1), 85–96.

Feyeux, N., Vidard, A., & Nodet, M. (2018). Optimal transport for variational data assimilation. *Nonlinear Processes in Geophysics*, *25*(1), 55–66.

Fisher, M., & Gürol, S. (2017). Parallelization in the time dimension of four-dimensional variational data assimilation. *Quarterly Journal of the Royal Meteorological Society*, *143*(703), 1136–1147.

Fréchet, M. (1948). Les éléments aléatoires de nature quelconque dans un espace distancié. In *Annales de l'institut henri poincaré* (Vol. 10, pp. 215–310).

Gaspari, G., & Cohn, S. E. (1999). Construction of correlation functions in two and three dimensions. *Quarterly Journal of the Royal Meteorological Society*, *125*(554), 723–757.

Gordon, N. J., Salmond, D. J., & Smith, A. F. (1993). Novel approach to nonlinear/non-gaussian bayesian state estimation. In *Iee proceedings f (radar and signal processing)* (Vol. 140, pp. 107–113).

Hamill, T. M. (2001). Interpretation of rank histograms for verifying ensemble forecasts. *Monthly Weather Review*, *129*(3), 550–560.

Hamill, T. M., Whitaker, J. S., & Snyder, C. (2001). Distance-dependent filtering of background error covariance estimates in an ensemble kalman filter. *Monthly Weather Review*, *129*(11), 2776–2790.

Hellinger, E. (1909). Neue begründung der theorie quadratischer formen von unendlichvielen veränderlichen. *Journal für die reine und angewandte Mathematik (Crelles Journal)*, *1909*(136), 210–271.

Houtekamer, P. L., & Mitchell, H. L. (1998). Data assimilation using an ensemble kalman filter technique. *Monthly Weather Review*, *126*(3), 796–811.

Houtekamer, P. L., & Mitchell, H. L. (2001). A sequential ensemble kalman filter for atmospheric data assimilation. *Monthly Weather Review*, *129*(1), 123–137.

Houtekamer, P. L., & Zhang, F. (2016). Review of the ensemble kalman filter for atmospheric data assimilation. *Monthly Weather Review*, *144*(12), 4489–4532.

Janjić, T., Nerger, L., Albertella, A., Schröter, J., & Skachko, S. (2011). On domain localization in ensemble-based kalman filter algorithms. *Monthly Weather Review*, *139*(7), 2046–2060.

Kalman, R. E. (1960). A New Approach to Linear Filtering and Prediction Problems. *Journal of Basic Engineering*. doi: 10.1115/1.3662552

Kalnay, E. (2003). *Atmospheric modeling, data assimilation and predictability*. Cambridge university press.

Kantorovich, L. V. (1942). On the translocation of masses. In *Dokl. akad. nauk. ussr (ns)* (Vol. 37, pp. 199–201).

Kapur, J. N. (1994). *Measures of information and their applications*. Wiley-Interscience.

Kolouri, S., Park, S. R., Thorpe, M., Slepcev, D., & Rohde, G. K. (2017). Optimal mass transport: Signal processing and machine-learning applications. *IEEE signal processing magazine*, *34*(4), 43–59.

Kullback, S., & Leibler, R. A. (1951). On information and sufficiency. *The annals of mathematical statistics*, *22*(1), 79–86.

Kutta, W. (1901). Beitrag zur naherungsweisen integration totaler differentialgleichungen. *Z. Math. Phys.*, *46*, 435–453.

Lei, L., Whitaker, J. S., & Bishop, C. (2018). Improving assimilation of radiance observations by implementing model space localization in an ensemble kalman filter. *Journal of Advances in Modeling Earth Systems*, *10*(12), 3221–3232.

Lguensat, R., Tandeo, P., Ailliot, P., Pulido, M., & Fablet, R. (2017). The analog data assimilation. *Monthly Weather Review*, *145*(10), 4093–4107.

Li, L., Vidard, A., Le Dimet, F.-X., & Ma, J. (2018). Topological data assimilation using wasserstein distance. *Inverse Problems*, *35*(1), 015006.

Li, R., Jan, N. M., Huang, B., & Prasad, V. (2019). Constrained ensemble kalman filter based on kullback–leibler divergence. *Journal of Process Control*, *81*, 150–161.

Li, T., Bolic, M., & Djuric, P. M. (2015). Resampling methods for particle filtering: classification, implementation, and strategies. *IEEE Signal processing magazine*, *32*(3), 70–86.

Li, Z., Zang, Z., Li, Q., Chao, Y., Chen, D., Ye, Z., ... Liou, K. (2013). A three-dimensional variational data assimilation system for multiple aerosol species with wrf/chem and an application to pm 2.5 prediction. *Atmospheric Chemistry and Physics*, *13*(8), 4265–4278.

Lin, L.-F., Ebtehaj, A. M., Flores, A. N., Bastola, S., & Bras, R. L. (2017). Combined assimilation of satellite precipitation and soil moisture: A case study using trmm and smos data. *Monthly Weather Review*, *145*(12), 4997–5014.

Lorenc, A., Ballard, S., Bell, R., Ingleby, N., Andrews, P., Barker, D., ... others (2000). The met. office global three-dimensional variational data assimilation scheme. *Quarterly Journal of the Royal Meteorological Society*, *126*(570), 2991–3012.

Lorenc, A. C. (1986). Analysis methods for numerical weather prediction. *Quarterly Journal of the Royal Meteorological Society*, *112*(474), 1177–1194.

Lorenz, E. N. (1995). Predictability-a problem partly solved. In *Predictability of weather and climate.* ECMWF. Retrieved from `https://www.ecmwf.int/node/10829` doi: 10.1017/CBO9780511617652.004

Lorenz, E. N., & Emanuel, K. A. (1998). Optimal sites for supplementary weather observations: Simulation with a small model. *Journal of the Atmospheric Sciences*, *55*(3), 399–414.

Maclean, J., Santitissadeekorn, N., & Jones, C. K. (2017). A coherent structure approach for parameter estimation in lagrangian data assimilation. *Physica D: Nonlinear Phenomena*, *360*, 36–45.

McCann, R. J. (1997). A convexity principle for interacting gases. *Advances in mathematics*, *128*(1), 153–179.

Monge, G. (1781). Mémoire sur la théorie des déblais et des remblais. *Histoire de l'Académie Royale des Sciences de Paris*.

Nerger, L., Janjić, T., Schröter, J., & Hiller, W. (2012a). A regulated localization scheme for ensemble-based kalman filters. *Quarterly Journal of the Royal Meteorological Society*, *138*(664), 802–812.

Nerger, L., Janjić, T., Schröter, J., & Hiller, W. (2012b). A unification of ensemble square root kalman filters. *Monthly Weather Review*, *140*(7), 2335–2345.

Ning, L., Carli, F. P., Ebtehaj, A. M., Foufoula-Georgiou, E., & Georgiou, T. T. (2014). Coping with model error in variational data assimilation using optimal mass transport. *Water Resources Research*, *50*(7), 5817–5830.

Orlin, J. B. (1993). A faster strongly polynomial minimum cost flow algorithm. *Operations research*, *41*(2), 338–350.

Pass, B. (2015). Multi-marginal optimal transport: theory and applications. *ESAIM: Mathematical Modelling and Numerical Analysis*, *49*(6), 1771–1790.

Pedlosky, J., et al. (1987). *Geophysical fluid dynamics* (Vol. 710). Springer.

Penny, S., Bach, E., Bhargava, K., Chang, C.-C., Da, C., Sun, L., & Yoshida, T. (2019). Strongly coupled data assimilation in multiscale media: Experiments using a quasi-geostrophic coupled model. *Journal of Advances in Modeling Earth Systems*, *11*(6), 1803–1829.

Peyré, G., Cuturi, M., et al. (2019). Computational optimal transport. *Foundations and Trends in Machine Learning*, *11*(5-6), 355–607.

Pitt, M. K., & Shephard, N. (1999). Filtering via simulation: Auxiliary particle filters. *Journal of the American statistical association*, *94*(446), 590–599.

Poterjoy, J., & Anderson, J. L. (2016). Efficient assimilation of simulated observations in a high-dimensional geophysical system using a localized particle filter. *Monthly Weather Review*, *144*(5), 2007–2020.

Poterjoy, J., & Zhang, F. (2014). Intercomparison and coupling of ensemble and four-dimensional variational data assimilation methods for the analysis and forecasting of hurricane karl (2010). *Monthly Weather Review*, *142*(9), 3347–3364.

Pulido, M., & van Leeuwen, P. J. (2019). Sequential monte carlo with kernel embedded mappings: The mapping particle filter. *Journal of Computational Physics*, *396*, 400–415.

Rabier, F., Järvinen, H., Klinker, E., Mahfouf, J.-F., & Simmons, A. (2000). The ecmwf operational implementation of four-dimensional variational assimilation. i: Experimental results with simplified physics. *Quarterly Journal of the Royal Meteorological Society*, *126*(564), 1143–1170.

Rabin, J., Peyré, G., Delon, J., & Bernot, M. (2011). Wasserstein barycenter and its application to texture mixing. In *International conference on scale space and variational methods in computer vision* (pp. 435–446).

Rao, C. R., Rao, C. R., Statistiker, M., Rao, C. R., & Rao, C. R. (1973). *Linear statistical inference and its applications* (Vol. 2). Wiley New York.

Reich, S. (2013). A nonparametric ensemble transform method for bayesian inference. *SIAM Journal on Scientific Computing*, *35*(4), A2013–A2024.

Reichle, R. H., McLaughlin, D. B., & Entekhabi, D. (2002). Hydrologic data assimilation with the ensemble kalman filter. *Monthly Weather Review*, *130*(1), 103–114.

Runge, C. (1895). Über die numerische auflösung von differentialgleichungen. *Mathematische Annalen*, *46*(2), 167–178.

Shen, Z., & Tang, Y. (2015). A modified ensemble kalman particle filter for non-gaussian systems with nonlinear measurement functions. *Journal of Advances in Modeling Earth Systems*, *7*(1), 50–66.

Sinkhorn, R. (1967). Diagonal Equivalence to Matrices with Prescribed Row and Column Sums. *The American Mathematical Monthly*. doi: 10.2307/2314570

Spiller, E. T., Budhiraja, A., Ide, K., & Jones, C. K. (2008). Modified particle filter methods for assimilating lagrangian data into a point-vortex model. *Physica D: Nonlinear Phenomena*, *237*(10-12), 1498–1506.

Srivastava, S., Li, C., & Dunson, D. B. (2018). Scalable bayes via barycenter in wasserstein space. *The Journal of Machine Learning Research*, *19*(1), 312–346.

Tagade, P., & Ravela, S. (2014). On a quadratic information measure for data assimilation. In *2014 american control conference* (pp. 598–603).

Tamang, S. K., Ebtehaj, A., Van Leeuwen, P. J., Zou, D., & Lerman, G. (2021). Ensemble riemannian data assimilation over the wasserstein space. *Nonlinear Processes in Geophysics Discussions*, 1–26.

Tamang, S. K., Ebtehaj, A., Zou, D., & Lerman, G. (2020). Regularized variational data assimilation for bias treatment using the wasserstein metric. *Quarterly Journal of the Royal Meteorological Society*.

Tang, Y., Deng, Z., Manoj, K., & Chen, D. (2014). A practical scheme of the sigma-point kalman filter for high-dimensional systems. *Journal of Advances in Modeling Earth Systems*, *6*(1), 21–37.

Tian, X., Zhang, H., Feng, X., & Xie, Y. (2018). Nonlinear least squares en4dvar to 4denvar methods for data assimilation: Formulation, analysis, and preliminary evaluation. *Monthly Weather Review*, *146*(1), 77–93.

Tippett, M. K., Anderson, J. L., Bishop, C. H., Hamill, T. M., & Whitaker, J. S. (2003). Ensemble square root filters. *Monthly Weather Review*, *131*(7), 1485–1490.

Trevisan, A., & Palatella, L. (2011). On the kalman filter error covariance collapse into the unstable subspace. *Nonlinear Processes in Geophysics*, *18*(2), 243.

Van Leeuwen, P. J. (2009). Particle filtering in geophysical systems. *Monthly Weather Review*, *137*(12), 4089–4114.

van Leeuwen, P. J. (2010). Nonlinear data assimilation in geosciences: an extremely efficient particle filter. *Quarterly Journal of the Royal Meteorological Society*, *136*(653), 1991–1999.

Van Leeuwen, P. J. (2020). A consistent interpretation of the stochastic version of the ensemble kalman filter. *Quarterly Journal of the Royal Meteorological Society*, *146*(731), 2815–2825.

Villani, C. (2003). *Topics in Optimal Transportation*. doi: 10.1090/gsm/058

Villani, C. (2008). *Optimal transport: old and new* (Vol. 338). Springer Science & Business Media.

Vissio, G., Lembo, V., Lucarini, V., & Ghil, M. (2020). Evaluating the performance of climate models based on wasserstein distance. *Geophysical Research Letters*, *47*(21), e2020GL089385.

Yang, Y., & Engquist, B. (2018). Analysis of optimal transport and related misfit functions in full-waveform inversion. *Geophysics*, *83*(1), A7–A12.

Yang, Y., Engquist, B., Sun, J., & Hamfeldt, B. F. (2018). Application of optimal transport and the quadratic wasserstein metric to full-waveform inversion. *Geophysics*, *83*(1), R43–R62.

Yong, P., Huang, J., Li, Z., Liao, W., & Qu, L. (2019). Least-squares reverse time migration via linearized waveform inversion using a wasserstein metric. *Geophysics*, *84*(5), S411–S423.

Zupanski, M. (1993). Regional 4-Dimensional Variational Data Assimilation in a Quasi-Operational Forecasting Environment. *Monthly Weather Review*, *121*(8), 2396–2408.